

1 **Dust Haze in Valles Marineris observed by HRSC and OMEGA onboard Mars**
2 **Express**

3

4 A. Inada¹, M. Garcia-Comas², F. Altieri³, K. Gwinner⁴, F. Poulet⁵, G. Bellucci³, H. U.
5 Keller², W. J. Markiewicz², M. I. Richardson¹, N. Hoekzema², G. Neukum⁶ and J-P.
6 Bibring⁵

7

8 1. California Institute of Technology, Pasadena, CA, U.S.A

9 2. Max-Planck-Institute of Solar System Research, Lindau, Germany

10 3. IFSI-INAF, Roma, Italy

11 4. DLR, Berlin, Germany

12 5. IAU, Universite Paris, Orsay, France

13 6. Freie Universitaet Berlin, Berlin, Germany

1 **Abstract**

2

3 We present analysis of a bright haze observed inside Valles Marineris, which formed in
4 mid northern spring. The data were collected by the High Resolution Stereo Camera
5 (HRSC) and the imaging spectrometer, Observatoire pour la Minéralogie, l'Eau, les
6 Glaces et l'Activité (OMEGA), aboard Mars Express. This study provides a case example
7 of the power of simultaneous multiple emission angle and hyperspectral imaging for
8 study of aerosols and clouds in the Martian atmosphere. The haze appeared thinner after
9 three days and disappeared in nine days. It was limited to a two-kilometer layer at the
10 bottom of the canyon. The color was redder than the underlying surface. The analysis of
11 the OMEGA spectra indicates that this haze was composed of dust particles. The dust
12 layer appeared brighter with the HRSC stereo channels than the nadir channel due to
13 longer scattering paths. We have estimated the optical depth of the haze by fitting both
14 HRSC and OMEGA data with radiative transfer calculations. The retrieval of the optical
15 depth is very sensitive to the aerosol scattering model used and the reflectance of the
16 surface. Applying an aerosol scattering model derived from sky surveys at a constant
17 elevation by the Imager for Mars Pathfinder, the optical depth of the haze is estimated
18 from HRSC data to be within 1.7 to 2.3 at the wavelength (λ) of 0.675 μm . The
19 wavelength dependence is obtained from OMEGA spectrum. It increases to 2.2-2.6 at λ
20 =1.35 μm and moderately decreases to 1.2-1.8 at λ =2.4 μm .

1 **1. Introduction**

2

3 Valles Marineris, located near the equator, is the deepest valley system on Mars. Its depth
4 reaches up to 8 km and its length extends from 270°E to 310°E. This great canyon affects
5 the atmosphere on a global scale. It is known that the main cloud belt appears constantly
6 over the valley in late northern spring and summer (or “aphelion season”) [*e.g. Wang and*
7 *Ingersoll, 2002*]. This region is also particularly interesting for the study of atmospheric
8 behavior on mesoscales due to the extreme variation of topography.

9

10 Although the high resolution stereo camera (HRSC) aboard Mars Express (MEX) has been
11 primarily designed to map the surface of Mars, it can also be used to study various
12 aspects of the Martian atmosphere [*Neukum and Jaumann, 2004*]. The stereo channels
13 detect the scattered light at five geometric angles with different path lengths. The angular
14 dependences of the surface and the aerosol scattering behaviors, as well as the optical
15 thickness of the atmosphere influence the stereo data. OMEGA (Observatoire pour la
16 Minéralogie, l’Eau, les Glaces et l’Activité), an imaging spectrometer on MEX, was
17 designed primarily to study surface mineralogy. It has identified a variety of mafic and
18 altered minerals [*Bibring et al., 2004; Bibring et al., 2006*] and H₂O / CO₂ ice on the
19 south polar cap [*Bibring et al., 2004*]. Moreover temperature and pressure at the surface
20 can be derived from the spectra [*Forget et al., 2007; Melchiorri et al., 2006*] , and, as it
21 will be shown here, also the composition of atmospheric features such as clouds or
22 hazes. The combination of these two instruments provides useful datasets for detailed
23 study of local weather on Mars that has been unavailable before the arrival of Mars
24 Express. Future spacecraft will have the ability to use the techniques described in this

1 paper – including the Mars Reconnaissance Orbiter. For example imaging data can show
2 the spatial distribution of atmospheric hazes, however it does not distinguish well
3 between water ice and dust particles. The spectrometer data, on the other hand, can
4 usually do this separation very well.

5

6 MEX was launched on 2nd June 2003 and arrived at Mars in December 2003. In the first
7 year of operation, the instruments observed a bright haze in Valles Marineris. The HRSC
8 data show the appearance of the haze to depend on time of day. The observations
9 motivated us to research a local atmospheric activity in short time scale to understand the
10 Martian atmosphere better in mesoscale level. The spectra taken with OMEGA show that
11 it consists of dust particles, although one may easily consider that it is a water ice fog.
12 The formation processes of the haze are still unknown, however, it seems plausible that
13 the haze could be generated inside the canyon due to strong winds. The detailed studies
14 of the dust haze will constrain the future work about examination of potential processes
15 of dust lifting. Besides, the spectral dependence of the reflectance measured over this
16 thick haze layer are dominated by the nature of the aerosols of which it is composed.
17 Therefore, the analysis of these measurements provide a chance to test the suitability and
18 the sensitivity for the aerosols involved in this specific scenario to several optical
19 property sets reported in the literature up to date. This kind of analysis thus constrains the
20 properties of the martian aerosols which may be extended to a variety of situations on
21 Mars. Here, we report on the characteristics and the estimated optical depth of the haze.
22 We describe the instruments in Section 2, and the observations in Section 3. In Section 4,
23 we show the characteristics of the haze such as composition, brightness temperature, the
24 wavelength and angular dependences of the haze reflectance, haze height, and optical

1 depth. The conclusions are summarized in Section 5.

2

3

1 **2. Instruments**

2

3 HRSC was developed at the German Aerospace Center (DLR), Germany, in cooperation
4 with German industry. It is a pushbroom scanner applying nine CCD line sensors
5 observing in four colors (Blue: 440 ± 45 nm, Green: 530 ± 45 nm, Red: 750 ± 20 nm, and
6 IR: 970 ± 45 nm) and five panchromatic stereo bands (675 ± 90 nm). During nominal
7 observations the camera is nadir pointing, and the angles of the channels from nadir are
8 18.9° (S1), 15.0° (IR) 12.8° (P1), 2.4° (Green), 0° (ND), -2.4° (Blue), -12.8° (P2), -15.0°
9 (Red), -18.9° (S2) along the track. In general all channels operate simultaneously; usually
10 pixels are summed into macro pixels for most channels to decrease the data volume
11 before transmission. An image has a swath of 62 km with the spatial resolution of 12
12 m/pixel at pericenter, and the minimum length of an image is about 330 km. At true
13 anomalies of $\pm 20^\circ$ the spatial resolution is ~ 15 m/pixel [*Neukum and Jaumann, 2004*].
14 The preflight radiometric calibration includes pixel response non-uniformity effects of
15 the optics, dark signal, CCD saturation behavior, spectral responsivity, camera sensitivity
16 to gain changes, integration time and macro-pixel format, signal dependence on
17 temperature, linearity with respect to illumination levels, stability with respect to
18 permutations of the CCD to signal chain allocation, temporal signal stability, and
19 sensitivity to electrical perturbations from outside the camera [*Jaumann et al., 2006*].
20 Imaging of the Earth and Moon during cruise has confirmed the on-ground calibration.
21 The signal noise ratio for panchromatic and color channels are larger than 100 and 80
22 respectively, except Blue with larger than 40.

23

24 OMEGA was developed through the collaboration of IAS (Institut d'Astrophysique

1 Spatiale, Orsay, France), LESIA (Laboratoire d'Etudes Spatiales et d'Instrumentation en
2 Astrophysique, Observatoire de Paris/Meudon, France), IFSI (Istituto di Fisica dello
3 Spazio Interplanetario, Rome, Italy), and IKI (Institute for Space Research, Moscow,
4 Russia). OMEGA can acquire images with a spatial resolution ranging from 300 m/pixel
5 to 5 km/pixel, depending on the position of the spacecraft on its elliptic orbit, and provide
6 for each pixel of the image a spectrum from wavelengths (λ) of 360 nm to 5100 nm with
7 352 channels. The mean spectral resolution is about 15 nm and the signal to noise ratio is
8 larger than 100 at all wavelengths. To cover the entire spectral range OMEGA uses three
9 separate channels: the visible and near-infrared channel VNIR, operating from $\lambda = 360$ to
10 1010 nm, and two infrared channels SWIR and LWIR, operating from $\lambda = 930$ to 2650
11 nm and 2510 to 5100 nm respectively [Bibring, 2004]. The detailed preflight calibration
12 setup is described in *Bonello et al.* [2005] and the radiometric absolute and relative
13 sensitivities are less than 20 % and 1 % respectively.

14

15

1 **3. Observations over Valles Marineris**

2
3 **3.1 The Season and the Local Time**

4
5 HRSC observed Valles Marineris on 25 May 2004 (the orbit number is 438), 28 May
6 2004 (449) and 3 June 2004 (471). The observation days, the areocentric solar longitudes
7 (L_s), the local times, and the geometric angles are summarized in Table 1. The images of
8 orbits 438 and 449, as well as those of orbits 449 and 471, overlap each other. They can
9 therefore provide information on weather changes within the canyon. The observations
10 were performed with all channels. The spacecraft moved from south to north, and S1, IR,
11 P1 and Green channels were forward looking while Blue, P2, Red and S2 were backward
12 looking.

13
14 OMEGA obtained spectra of the same region and at the same time as HRSC on 25 May
15 2004 (*i.e.*, during orbit 438). On orbits 460 (acquired on 31 May 2004) and 482 (6 June
16 2004) images of Valles Marineris were also taken by OMEGA (Table 1), though they
17 were not overlapped and they were not taken simultaneously by HRSC. These were
18 nominal nadir mode observations.

19
20 All images were taken in the morning, at the local time of around 9 A.M. The difference
21 in illumination angles is little, and hence it does not affect the comparison of the images.
22 The images were collected at the beginning of the aphelion season ($L_s=40^\circ$) before the
23 tropical cloud belt had extended over the valley [*Smith et al., 2001; Smith, 2004; Wang*
24 *and Ingersoll, 2002*].

1

2 **3.2 Brightness Change in Valles Marineris**

3

4 Figure 1 shows the HRSC orthoimages of Valles Marineris, including the haze, that have
5 been map-projected using the high-resolution HRSC digital terrain model (DTM)
6 [Gwinner *et al.*, 2005]. HRSC level 4 orthoimages [Scholten *et al.*, 2005] are map-
7 projected images in which geometric distortions due to topography have been eliminated
8 using the underlying HRSC DTM. The level 4 data are resized for a suitable spatial
9 resolution by averaging I/F of some pixels on the original images depending on macro-
10 pixel setting. This method increases radiometric accuracy typically by factor of 10 for
11 ND data that are generally obtained without the macro-pixel mode. The lines in the
12 Figure 1 mark overlap areas between orbits 438 and 449 (white), and 449 and 471 (red).
13 They correspond to longitudes of 301.2°E and 298.7°E respectively.

14

15 Due to the large optical depth of the haze, the observed contrast inside the valley during
16 orbit 438 is significantly decreased and the atmospheric haze shows up quite brightly (the
17 right panel of Figure 1). The middle panel displays an image of the same region, but
18 slightly west, acquired three days later during orbit 449. There is a haze inside the valley
19 as well, but it is relatively thinner. Six days later, as it can be seen in the HRSC image
20 taken during orbit 471, the haze had disappeared or was too thin to detect (the left panel).

21

22 Figure 2 quantitatively presents the brightness change in the valley obtained with the
23 Green channel, which represents the typical behavior of all channels. I/F profiles along
24 the white lines of Figure 1 detected during orbits 438 and 449 are shown with the solid

1 and dashed lines respectively in the left panel of Figure 2. Henceforth, I/F is defined as
2 the ratio of the detected intensity to intensity reflected from a perfect Lambert surface
3 illuminated at the zenith angle of zero degree. The right panel shows I/F of orbit 449 with
4 the solid line and 471 with the dashed line. The altitude of the surface is plotted with the
5 dotted lines as a reference. Latitudes between 13°S and 14°S correspond to the interior of
6 Valles Marineris, where I/F is larger due to the haze than outside of the valley on orbits
7 438 and 449. Moreover, the haze observed on orbit 438 is brighter than on orbit 449. Also
8 the difference in I/F between the images of orbits 449 and 471 is prominent in the valley.

9

10 These observations can be interpreted as the haze becoming thinner and disappearing
11 during nine days or, alternatively, that the haze disappeared and reappeared daily, but not
12 always with the same thickness.

13

14

15 **3.3 Spectrum Comparison with HRSC and OMEGA in Visible Wavelength**

16

17 We compared the spectra from two regions of the inside of the canyon (13.75°S-14.00°S,
18 302.0°E-302.5°E) and a region north of the canyon (12.00°S-12.25°S, 302.0°E-302.5°E)
19 obtained by HRSC and the OMEGA visible bands on orbit 438. The comparison provides
20 excellent information about the absolute calibrations of the instruments because the data
21 sets were acquired at the same time, in which the incidence angles were the same and the
22 atmosphere was unique. The sub-regions are shown as the insides of the rectangles on
23 Figure 1. OMEGA spectra of the inside and to the north of the canyon are given with the
24 solid and dashed lines respectively in Figure 3, while the mean I/F of HRSC are with the

1 asterisks and diamonds.

2

3 Inside Valles Marineris, the detected I/F by HRSC is larger than that by OMEGA except
4 at $\lambda = 0.675 \mu\text{m}$, for which the data with the nadir channel are used. The HRSC data do
5 not contain any angular correction; hence the I/F difference is likely due to the longer
6 viewing path in the bright dust haze. The panchromatic filters have a wide spectral width
7 of $0.18 \mu\text{m}$, and the brightness as evidenced by OMEGA decreases steeply from the
8 center wavelength toward the shorter wavelengths within the filter width. Therefore it is
9 natural that the HRSC nadir data shows lower I/F than OMEGA. The measurements at
10 this wavelength are, however, within OMEGA and HRSC one-sigma values.

11

12 The data without the dust haze are more suitable to use for radiometric calibration. The
13 response of the HRSC Blue channel is identical to those of the OMEGA I/F at the same
14 wavelength as the ratio of HRSC I/F to OMEGA I/F ($R_{H/O}$) is 1.04. The HRSC Green and
15 Red channels are brighter than the OMEGA data as $R_{H/O} = 1.18$ and 1.23 respectively,
16 while the brightness of the HRSC infrared channel is within the one-sigma of the
17 OMEGA spectral data with $R_{H/O} = 0.974$.

18

19 The trend of our results is similar to the previous report [*McCord et al.*, 2007] except for
20 the Green band. They compared HRSC color spectra with those from both the OMEGA
21 visual channel and Earth-based telescope measurements for radiometric calibrations. The
22 reflectance of the HRSC Blue, Green and IR channels agree in that of OMEGA and
23 telescopes, while the HRSC Red I/F is systematically larger than the others. The average
24 $R_{H/O}$ for Blue, Green, Red and IR on orbits 97, 334 and 360 data are 0.97 ± 0.02 ,

1 1.07±0.02, 1.10±0.03, and 0.97±0.04 respectively. The differences are partially due to
2 scattering from the atmosphere and the surface in the different viewing geometries.
3 However images of Phobos, which has no atmosphere, with the HRSC Red channels
4 having similar offsets from OMEGA data implies that an instrument calibration
5 adjustment may be needed.

6

7 The $R_{H/O} = 1.23$ at the wavelength of $0.675 \mu\text{m}$ in our data is even larger than the
8 previously reported $R_{H/O} = 1.10$. We attribute the differences mainly to the different
9 observation geometries. The phase angles (g) of the north region are 38.12 deg. for the
10 HRSC red channel. Back scattering is usually dominant for the surface, by comparison
11 with imaging of the Moon [*Hillier et al.*, 1999]. Hence I/F of the HRSC Red is expected
12 to be larger than OMEGA I/F that was observed at nadir with $g = 48.0$ deg., unless the
13 atmosphere is sufficiently optically thick so as to mask the surface angular behavior. The
14 angular dependence of reflectance is further discussed in the next section. Although the
15 reason why the HRSC Green channel is brighter over the surface than the OMEGA data
16 in spite of the slightly larger phase angle (2.0 deg.) is still unclear, we conclude that the
17 data collected by the two instruments agree reasonably with each other.

1 **4. Characteristics of the Haze**

2

3 **4.1 Composition of the Haze**

4

5 The spectra taken by OMEGA during orbit 438 (Figure 3) provide insight into the
6 composition of the haze seen in the HRSC images in Valles Marineris. The data are
7 corrected for thermal emission as described by *Jouglet et al.* (2006) and for atmospheric
8 gaseous absorptions as described by *Langevin et al.* (2005) .

9

10 We have examined the OMEGA spectra for spectral features typical of the atmospheric
11 aerosols most likely responsible for the increase in reflectance seen by HRSC inside the
12 canyon. In order to discriminate airborne dust from aerosol ices, we calculated the
13 relative band depth at 1.43 and 1.5 μm , wavelengths where CO_2 and H_2O ices
14 show prominent absorption features [*Clark, 1981; Gerakines et al., 2005;*
15 *Warren, 1984*], we estimated the total water band depth and the water
16 content at 3.0 μm , where H_2O ice strongly absorbs [*Bell et al., 1996*], and we
17 mapped the spectral slope in the near-infrared.

18

19 The relative band depth at a specific wavelength λ is generally written as

20

21
$$D = 1.0 - r(\lambda)/r_c \quad (1)$$

22

23 where $r(\lambda)$ is I/F at the wavelength λ and

24

1
$$r_c = (1.0-f) r(\lambda_1) + f r(\lambda_2) \quad (2)$$

2

3 λ_1 and λ_2 are the wavelength of the two points chosen for the local continuum and

4

5
$$f = (\lambda - \lambda_1) / (\lambda_2 - \lambda_1) \quad (3)$$

6

7

8 The relative band depth is a diagnostic for the presence of atmospheric and surface
9 constituents. A correct interpretation of the calculated relative band depths relies on an
10 adequate selection of the continuum points. We have carefully chosen the wavelengths
11 for the local continuum to avoid atmospheric and surface absorption features.

12

13 The band at $\lambda = 1.43 \mu\text{m}$ corresponds to absorption from CO_2 ice and gas. Figure 4-1-a
14 shows a 2-D map of the band depth relative to a local continuum at $\lambda_1 = 1.39 \mu\text{m}$
15 and $\lambda_2 = 1.44 \mu\text{m}$ for the portion of orbit 438 taken by OMEGA over Valles Marineris.
16 The results are also plotted for orbit 482 to have a reference scenario without haze
17 (Figure 4-1-b). OMEGA spectra present a slightly stronger absorption for lower altitudes,
18 especially for orbit 482 inside the valley. This feature could be attributable to errors in the
19 estimated CO_2 column density used to correct the data for gas absorptions and not to CO_2
20 ice absorption. Besides, the fluctuations in band depth within one orbit are smaller than
21 2%, which should not be taken as an evidence of absorption but probably being due to the
22 instrumental and calibration errors. Therefore, we take the $1.43 \mu\text{m}$ band depth maps of
23 both orbits to show no CO_2 ice absorption.

24

1 The relative band depth at $\lambda = 1.50 \mu\text{m}$ for orbit 438 data is shown in Figure 4-2-a. A
2 similar map for orbit 482 is also shown in Figure 4-2-b for comparison. In this case, we
3 have chosen $\lambda_1 = 1.30 \mu\text{m}$ and $\lambda_2 = 1.71 \mu\text{m}$ as the local continuum wavelengths. This
4 band is sensitive to atmospheric water ice particles especially those which radii are larger
5 than $\sim 5.0 \mu\text{m}$. Although OMEGA relative calibration error is less than 1%, some
6 hysteresis affect the accuracy in the wavelength region of 1.0-1.4 μm . Hence, to account
7 for instrumental and atmospheric biases, we consider that the water ice feature in this
8 absorption band has to be larger than 2% to be taken as a positive detection and therefore
9 larger than the instrumental noise. If water ice clouds were present, the band depth would
10 be larger than under clear atmospheric conditions. On the contrary, the maps shown in the
11 figures look homogeneous and shows band depths smaller than 2% across the whole
12 plotted area. This indicates no correlation between H₂O ice and the bright feature
13 detected in the visible wavelengths.

14

15 The 3.0 μm band is a deeper and wider H₂O ice band than the one at 1.50 μm , in which
16 both absorptions from surface hydrated minerals and atmospheric H₂O ice particles
17 contribute. This absorption band is more sensitive to the water ice particles with radii of
18 smaller than $\sim 3.0 \mu\text{m}$ than the 1.5 μm band [see, e.g., *Pimentel et al.*, 1974]. However,
19 the water ice absorption in this band overlaps the surface hydration band and thus, to
20 confidently rule out ice presence, both bands should be checked. Due to the non linearity
21 of the instrument in this wavelength region, we consider that OMEGA detects water ice
22 particles when the variation in the absorption at the 3.0 μm band is more than 3.0%.
23 Figure 4-3 shows the hydration estimated for orbits 438 and 482 by an integration of the
24 band depth between a continuum and the spectrum from 3.0 to 3.7 μm , as described in

1 *Jouglet et al.* [2006]. A method to retrieve the water mass proportion has been proposed
2 by *Yen et al.* [1998], which is based on spectra measurements of Martian-like samples
3 with several hydration rates in laboratory. The results estimated using a similar method
4 are presented in Figure 4-4. It shows that there is not a significant variation of water
5 content (less than 3.0%) between regions inside and outside the canyon. The water
6 content maps even show slightly smaller values inside the valley when the haze was
7 present (orbit 438). In any case, with such small variations of water content, it can be said
8 that no water ice in the atmosphere was detected during these observations. We therefore
9 rule out H₂O ice as main component of the haze monitored inside Valles Marineris.

10

11 The spectral slope (“reddening”) in the near-infrared (NIR) is related to aerosol
12 presence, in particular, to dust. In the NIR, the surface albedo weakly depends on
13 wavelength (with the exception of polar regions), *i.e.*, the spectrum of the surface
14 component is more or less flat. However, the dust extinction cross section generally
15 decreases with wavelength (at least beyond around 1.2-1.4 μm for the Martian dust, being
16 that wavelength dependent on the particle size distribution). As a consequence, when dust
17 particles are added to the atmosphere, the spectrum becomes steeper [*Drossart et al.*,
18 1991; *Erard et al.*, 1994]. This is also expected for water ice particles with the effective
19 particle radii of $\sim 1.0 \mu\text{m}$. We define here the reddening as the ratio of reflectance at 1.26
20 μm to that at 2.49 μm . The reddening 2-D plots for orbits 438 and 482 over the canyon
21 are shown in Figure 4-5. The footprints with topographic slopes larger than 17% (walls of
22 the valley and abrupt regions) have been removed to avoid dependence of spectral slope
23 on observation geometry [*Combes et al.*, 1991]. A correlation between the reddening and
24 the aerosols seen in the HRSC and visible OMEGA data is noted. The ratio is clearly

1 larger for orbit 438 inside the canyon than that for orbit 482. Therefore, since we have
2 already ruled out the possibility of ice particles from the data, we conclude that the
3 composition of the haze is most likely dust.

5 **4.2 Valles Marineris Temperatures**

6
7 Another hint of ice non-presence can be inferred from the temperature. We derived the
8 brightness temperature at the local time of 08:57 (orbit 482), 09:07 (460) and 09:15 (438)
9 from the OMEGA spectrum at the wavelength of 5.0 μm . Those of the inside of the
10 canyon and the outside (north of Valles Marineris) are plotted as a function of local time
11 in Figure 5. The temperatures are the averaged values in 0.1 x 0.1 deg. boxes at the
12 longitudes of 302.10°E, 298.94°E, 298.73°E for orbit 438, 462, and 482 respectively. The
13 temperature outside of the canyon shows an increasing trend with the local time, mainly
14 due to an increase in the surface temperature as the sun rises. However the inside of the
15 canyon on orbit 438 remains colder than orbit 460 – the latter orbiting being at an earlier
16 local time. This is because the brightness temperature in the canyon observed during orbit
17 438 is strongly affected by the temperature of the colder haze layer.

18
19 Although the dust layer is colder than the surface would be if the haze layer were not
20 present, the brightness temperature is still 223.77 ± 0.53 K. Since the dust haze is thick
21 and it forms at low altitudes as shown in Section 4.4, it can be considered that the
22 temperature of the haze is dominant in determining the brightness temperature. In this
23 case, it is too warm to expect any water ice particles on the basis of reasonable water
24 vapor mass mixing ratio estimates, which supports the idea that the haze is composed of

1 dust.

2

3 **4.3 Wavelength and Angular Dependences of the Haze**

4

5 We compared the haze color in the overlap regions of the HRSC images. Two areas were
6 selected: the first, at $14.25\pm 1.75^\circ\text{S}$, $301.20\pm 0.50^\circ\text{E}$, imaged during orbits 438 and 449
7 (hereafter referred as region 1), and the second, at $13.50\pm 1.50^\circ\text{S}$, $298.70\pm 0.50^\circ\text{E}$, was
8 imaged during orbits 449 and 471 (region 2). The center longitudes are indicated with the
9 white (region 1) and red (region 2) lines in Figure 1. These are the different regions from
10 the areas that we used for the spectra comparison between HRSC and OMEGA, because
11 we have to select overlap regions of the HRSC data taken on different orbits for this
12 purpose. We used only pixels corresponding to surface elevations of less than -5000 m
13 for the color analysis.

14

15 The color slopes of the considered regions are shown in Figure 6. Region 2, which
16 includes dust haze (orbit 449), has a markedly different wavelength dependence from the
17 surface in the absence of haze (orbit 471 image). The ratio $R = r(0.75) / r(0.44)$ increases
18 from 2.8 (clear atmosphere) to 3.1 (with the dust). The haze is thicker in region 1 on the
19 same image (449) and $R = 3.3$. This suggests that dust particles redden the total radiance
20 in visible wavelength. The haze observed on orbit 438 is even thicker and brighter than
21 on orbit 449, however, the color ratio r is the same.

22

23 Figure 7 shows color-composite stereo views of regions 1 observed on orbits 438 and 449
24 and region 2 obtained on orbits 449 and 471. These were created using panchromatic

1 channels as red for S1, green for nadir and blue for S2. The phase angles are 36.3 (S2),
2 46.0 (ND) and 62.4 (S1) deg. for region 1 on orbit 438 respectively, while they are 40.7,
3 50.9 and 66.9 deg. for region 1 on orbit 449. In region 2 the angles are 34.7 (S2), 43.7
4 (ND) and 60.4 (S1) deg. for orbit 449, and 43.0 (S2), 53.2 (ND) and 69.1 (S1) deg. for
5 orbit 471. There is an obvious false color difference between the inside and outside of the
6 canyon, highlighting different angular dependences. The bluish surface indicates the
7 strong back scattering.

8

9 The angular dependence of I/F for the haze and the surface are given in Figure 8. These
10 areas are marked as the white boxes ($0.3^\circ \times 0.2^\circ$) on Figure 7. In each region 1 and 2, we
11 have selected two sub-areas for the haze and the surface. Only the data from the
12 panchromatic channels were analyzed to avoid wavelength dependence. The brightness of
13 the haze in region 1 slightly increases with increasing emission angle (e), which is due to
14 the longer path length in the haze (Figure 8-a). The thinner haze in region 2 (orbit 449)
15 also shows minimum I/F at the smallest e , *i.e.*, with the shortest path length. The surface
16 scattering function plotted against e for the HRSC image data obtained on orbit 438 has a
17 strange zigzag pattern (Figure 8-b). It is due to the surface phase function that is not
18 masked by the thin atmospheric opacity. This is not seen in data from other orbits
19 because P1 and P2 data are not available. On the other hand, the increase in I/F at small
20 phase angles is clearly presented (Figure 8-d), which is expected from the lunar surface
21 scattering behavior. I/F from the bottom of the canyon detected during orbit 471 also
22 shows a backscattering component, while the reflectance of the haze displays no clear
23 dependence on phase angle (Figure 8-c). The effect of the thick dust haze on the angular
24 dependence of its reflectance surpasses those of the surface.

1

2 **4.4 Height of the Haze**

3

4 The height of the haze is derived using a high-resolution digital terrain model (DTM)
5 produced from the HRSC stereo data of orbit 438. We found that the edge of the haze
6 where it contacts the north wall can be identified as pixels of $0.0445 < I/F < 0.0460$ in the
7 blue image (Figure 9). The surface is usually dark and little contrast in the blue images,
8 therefore it is easier to distinguish haze using I/F in this channel than with the other color
9 images. The edge of the haze against the southern wall is difficult to define due to direct
10 sunlight and so only the height on the northern wall was calculated. Using this method
11 even in the north, it is possible that some pixels representing the surface could be
12 mistaken for haze since the topography of the canyon wall causes reflections that can fall
13 inside of the I/F range. To obtain a conservative estimate of haze altitude, when several
14 "in range" pixels are at the same longitude, we measured the height of the southern most
15 pixel (*i.e.* the one furthest from the wall) as the main haze edge. Figure 10 shows a cross
16 section of the north wall of the canyon at longitude of 302°E . The arrows represent the
17 boundary of the haze. The height along the longitude is given in Figure 11. The mean
18 height is -4172 ± 531 m, *i.e.*, about 1-2 km above the height of the bottom of the canyon.

19

20 **4.5 Optical Depth**

21

22 The optical depth (τ) of the haze for both datasets (HRSC and OMEGA) was derived by
23 using SHDOM (Spherical Harmonics Discrete Ordinates Model), a multiple scattering
24 radiative transfer code [Evans, 1998]. We have considered the atmosphere as a single

1 layer of dust particles. The code requires as input the observational geometry (provided
2 by HRSC and OMEGA), the dust optical properties, and the contribution of the radiation
3 reflected by the surface to the total reflectance.

4

5 We have considered three aerosol scattering models after *Markiewicz et al.* [1999]
6 (Model M), *Tomasko et al.* [1999] (Model T) and *OckertBell et al.* [1997] (Model O).
7 The first two models were derived from observations with the Imager for Mars Pathfinder
8 (IMP). The first used images along the great circle joining the north and south horizons to
9 the zenith, while the second used sky surveys images at a constant elevation. The third
10 was derived from Viking Lander, Phobos-2, and telescopic measurements. *Markiewicz et*
11 *al.* [1999] obtained the dust size distribution as the effective particle radius (r_{eff}) of 1.60
12 μm and the effective variance (v_{eff}) of 0.15 at $\lambda=0.67 \mu\text{m}$ with the modified gamma size
13 approximation, while *Tomasko et al.* [1999] derived $r_{\text{eff}} = 1.6 \pm 0.15 \mu\text{m}$ with a fixed v_{eff}
14 of 0.2 or 0.5. *Ockert-Bell et al.* [1997] employed $r_{\text{eff}} = 1.85 \mu\text{m}$ and $v_{\text{eff}} = 0.51$ derived by
15 *Pollack et al.* [1995]. With Model M, we use the phase function that *Markiewicz et al.*
16 [1999] derived directly from the IMP data, while for Models T and O, we approximate
17 the phase functions with the one-term Henyey-Greenstein model using their asymmetry
18 factors (Figure 12). This approximation fits the originally retrieved-phase functions
19 poorly in the forward scattering peak ($g > \sim 150^\circ$) and not very well in the backward
20 scattering region ($g < \sim 30^\circ$); nevertheless this little affects the retrieval of optical depth in
21 our case, mainly because the Henyey-Greenstein phase function is a good approximation
22 to the true function for phase angles within the range corresponding to our observations
23 ($38^\circ < g < 65^\circ$). The Henyey-Greenstein phase functions of Models T and O provide a
24 rather similar phase function in the range of these observed phase angles, although they

1 are larger than from Model M. The dust single scattering albedo (ω) and the asymmetry
2 factor (θ) of the phase functions are shown in Figure 13. The single scattering albedo
3 interpolated at $\lambda=0.675 \mu\text{m}$ after Model T ($\omega = 0.95$) is 2 % larger than the others ($\omega =$
4 0.93). Considering also the difference in the single scattering albedo, the dust particles of
5 Model M less effectively scatter than those of the other two dust models for our
6 observational geometries. Model O provides dust optical properties in a wavelength range
7 containing OMEGA spectral coverage completely. For applying Models M and T, we
8 need to expand the wavelength range. Based on results from the analysis of MGS TES
9 observations [Clancy *et al.*, 2003], we have assumed that ω and θ remain constant for $\lambda >$
10 $0.965 \mu\text{m}$.

11

12 We estimated the Lambertian albedo (A_L) of the surface below the haze with data taken
13 after the haze disappeared on orbits 471 and 482 for HRSC and OMEGA, respectively. In
14 reality the surface is not Lambertian, as it is shown in Figure 8-d. Although the HRSC
15 nadir and two stereo channel data are available, three data points are not enough to derive
16 an accurate surface phase function. However, we focus here on the haze optical depth
17 and, as the observational geometries for the two pairs of orbits 438-471 (HRSC) and 438-
18 482 (OMEGA) are similar, the effect of considering a surface different from Lambertian
19 on the derived τ is small. This is similar to considering the derived A_L as some effective
20 albedo for the specific observation geometry. First we estimated A_L by assuming dust-
21 free atmosphere in the data taken on orbits 471 and 482. Hereafter the models with this
22 Lambert albedo and the three aerosol models are referred to as Models M-1, T-1 and O-1.
23 The uncertainty from the assumption should be also considered since (1) dust particles
24 are always suspended in this region and (2) dust above dark surfaces such as at the

1 bottom of Valles Marineris usually enhances the total reflectance. Therefore we adopted τ
2 $=0.5$ as a reasonable optical depth and 1.0 as a dusty case at $\lambda=0.67 \mu\text{m}$ to estimate the
3 range of Lambert Albedo. The models with these A_L values and the three aerosols models
4 are referred as Models M-2, T-2 and O-2 for $\tau =0.5$ and M-3, T-3, and O-3 for $\tau =1.0$.
5 The applied models are summarized in Table 2.

6

7 Whereas HRSC has the ability to measure at the same wavelength in the five
8 panchromatic channels (therefore, providing reflectance at different phase angles),
9 OMEGA measures simultaneously at 352 wavelengths providing different wavelength
10 information. We describe below the method used for each dataset and the derived optical
11 depth.

12

13 **4.5.1 Retrieval of Optical Depth with HRSC Data**

14

15 We analyzed the HRSC panchromatic channels to estimate the optical depth of the dust
16 haze. The Lambert albedo of the surface below the haze is calculated from the averaged
17 reflectance at the bottom of the canyon in region 2 obtained on orbit 471, when the
18 atmosphere was relatively clear. The estimated A_L from the data of S1, nadir and S2 are
19 0.16 , 0.15 and 0.17 respectively. In order to derive the optical depth for the haze, we only
20 use A_L derived for the nadir channel.

21

22 First we applied Model M-1. Figure 14-1-a shows the results of the I/F simulations using
23 $A_L = 0.15$ for optical depths from 0 to 5, together with the observed I/F in region 1
24 acquired during orbit 438. A unique optical depth does not simultaneously fit all the

1 panchromatic data well. In this case, the nadir data suggests that the dust haze τ_m is 3.6,
2 while the S1 data at a larger phase angle shows smaller optical depth ($\tau_m = 3.0$) and the
3 S2 data at a smaller phase angle is better fitted with $\tau_m = 4.6$. This could be due to two
4 effects: (1) the brightness of the surface at small (large) phase angles is actually larger
5 (smaller) than the radiance calculated with the Lambert assumption, and/or (2) the dust
6 particles in the canyon have a larger backscattering component than the applied phase
7 function.

8

9 Figure 14-1-b shows the contour map of I/F calculated with the geometric angles of the
10 nadir data in region 1 of orbit 438. The incidence angle (i) is 49.4 deg., $e=3.79$ deg., and
11 $g = 46.0$ deg. Applying Model M-2, which assumed the optical depth is 0.5 on orbit 471,
12 A_L is 0.14, and the observed I/F of 0.142 corresponds to $\tau_m = 3.7$. The minimum τ_m is 3.6
13 with $A_L = 0.15$. The maximum could be 5.0 if $A_L = 0.0$, however even when we assume
14 dusty atmosphere on orbit 471 (Model M-3), $A_L=0.12$ and $\tau_m = 3.9$. Hence hereafter we
15 consider that the maximum τ_m is derived with Model M-3.

16

17 In the same manner, Models T and O are also applied. The results are shown in Figures
18 14-2 and 14-3 respectively. The estimated optical depths are smaller than Model M,
19 which less effectively scatters for this wavelength and geometry than the others. The
20 optical depth of the dust haze on orbit 438 derived with Model T is within the range from
21 1.7 ($A_L = 0.15$ with Model T-1) to 2.3 ($A_L = 0.08$ with Model T-3), while that with Model
22 O is between 1.9 ($A_L = 0.15$ with Model O-1) and 2.1 ($A_L = 0.07$ with Model O-3) (Table
23 2). Taking into account that the main difference between three dust models comes from
24 the different single scattering albedos, it is understandable that τ_m is larger than τ_t ,

1 however the former should be similar to τ_o . We derive τ_m larger than τ_o because the
2 aerosol phase function of Model M is slightly larger than Model O for the phase angles of
3 our observations. These tests show the retrieval of the optical depth to be very sensitive to
4 the aerosol model used, and the error in the optical depth caused by assuming Lambert
5 Albedo is smaller than the difference between the optical depths derived with each
6 scattering model.

7

8

9 **4.5.2 Retrieval of Optical Depth with OMEGA Data**

10

11 We have derived the optical depth for the haze detected on orbit 438 at wavelengths from
12 0.6 to 2.5 μm from OMEGA data with a similar approach. We averaged the radiance for
13 each spectrum from measurements taken over the bottom of the canyon from 13.76°S-
14 14.12°S and 301.7°E-302.6°E for orbit 438, and from 12.57°S-12.96°S and 296.9°E-
15 297.8°E for orbit 482. The average reflectance spectra for both orbits and those corrected
16 for the incidence angle are shown in Figure 15.

17

18 The optical depths on orbit 482 (after the dust haze disappeared) are assumed to be 0.5
19 for Models M-2, T-2 and O-2, and 1.0 for Models M-3, T-3 and O-3 at $\lambda=0.67 \mu\text{m}$, and
20 we have estimated τ for the rest of the wavelength range scaling with the extinction
21 efficiency factor (Q_{ext}) dependence, considered constant at $\lambda > 0.965 \mu\text{m}$ in Models M
22 and T. The derived albedos with the dust-free assumption, Models M-2, T-2 and O-2, and
23 Models M-3, T-3 and O-3 are given in Figure 16. The albedos derived considering dust
24 presence in orbit 482 are smaller than the one derived using a free atmosphere (at least at

1 $\lambda > 0.6 \mu\text{m}$), given Valles Marineris low albedo (relative to Mars average albedo). That
2 means that all three types of dust enhance the reflectance. However, the effect of the dust
3 on the albedo wavelength dependence in the case of Models O-2, O-3 and M-3 is not as
4 expected. For example, the relative difference between the albedo of Model O-2 and that
5 of the dust free case is around five times more at $\lambda = \sim 2.2 \mu\text{m}$ than at $\lambda = 0.67 \mu\text{m}$, and
6 from six to seven times more in the case of Models O-3 and M-3. This is not likely to be
7 correct since the contribution from Martian dust in the NIR should decrease as the
8 wavelength increases [see e.g. Clancy et al., 2003, Fig. 7.a; Drossart et al., 1991, Fig.
9 4.1.], and therefore the relative differences mentioned above should have a negative
10 spectral slope. This unexpected behavior could be due to too high of an optical depth or
11 to the use of dust that is too bright at $\lambda > 1.4 \mu\text{m}$ relative to the shorter wavelengths. The
12 case is similar for the surface albedo derived using Model M-2, although in this case the
13 dust seems too bright for $\lambda > 0.896 \mu\text{m}$ relative to the shorter wavelengths. The surface
14 albedo behavior derived using Models T-2 or T-3 seems more reasonable than the one
15 derived with the other two dust models, although the contribution from the aerosols is
16 also slightly larger for larger wavelengths in the NIR, in particular when the assumed
17 optical depth is 1.0, *i.e.*, T-3. This is also an indication of the dust model being too bright
18 or, more likely, to too large of an optical depth in those wavelengths. The reason for the
19 latter could be an erroneous Q_{ext} at $\lambda > \sim 1.35 \mu\text{m}$, considered here constant but which is
20 shown in the literature to slightly decrease towards longer wavelengths for the case of
21 Martian dust [see *e.g.*, Clancy et al., 2003].

22

23 After deriving A_L , we have retrieved the haze optical depth detected on orbit 438
24 considering the nine models. First we applied Model O-1 because the scattering

1 properties fully cover the OMEGA wavelength region. Figure 17-1 shows the retrieved
2 dust optical depth for Model O-1 and the error in the results. We estimated this error by
3 calculating the maximum and minimum optical depth at each wavelength that can be
4 retrieved according to the optical property error range in *Ockert-Bell et al.* [1997], *i.e.*,
5 $\pm 2\%$. The optical depth abruptly decreases from 2.5 at $\lambda = \sim 0.6 \mu\text{m}$ to 1.1 at $\lambda = 1 \mu\text{m}$.
6 Then, it remains almost constant up to $1.25 \mu\text{m}$ and smoothly decreases beyond to a value
7 of 0.6 at $\lambda = 2.5 \mu\text{m}$. This optical depth is inconsistent with Q_{ext} provided in *Ockert-Bell*
8 *et al.* [1997]. By definition, τ must scale linearly with Q_{ext} , *i.e.*, the ratio τ/Q_{ext} should
9 remain constant with wavelength. However, even within the error range, the ratio slope is
10 clearly negative, especially at visible wavelengths (see Figure 17-2).

11

12 The results with Models O-2 and O-3 are shown in Figure 18-1. As Model O-1, the
13 optical depth retrieved at $\lambda = 0.6 \mu\text{m}$ is also too large with respect to the NIR. This is
14 better illustrated in Figure 18-2, where we plot the ratio τ/Q_{ext} . Although the results
15 improve those derived using Model O-1, τ/Q_{ext} with Model O-2 still presents a very
16 pronounced negative slope in the visible, when it should be flat. This also happens with
17 Model O-3. The behavior beyond $1 \mu\text{m}$ in these two cases is reasonable, since the ratio
18 remains almost constant. Therefore, the kind of dust which is present in the observed
19 haze contributes to the total reflected radiance relatively more in the visible wavelength
20 than the dust of Model O, *i.e.*, its single scattering albedo/asymmetry parameter is
21 larger/smaller in the visible wavelength (relative to those in the NIR) than Model O. In
22 other words, the set of optical properties (single scattering albedo, phase function
23 asymmetry parameter, and extinction efficiency factor) provided by *Ockert-Bell et al.*
24 [1997] is not suitable for this haze in Valles Marineris for the whole wavelength range

1 from 0.6 to 2.5 μm .

2

3 Next, we applied Model M-1 in the same way. Figures 18-1 to 18-2 show the retrieved
4 optical depth and the ratio of τ/Q_{ext} respectively. At 0.675 μm , the optical depth equals
5 4.1 and doubles that derived with Model O-1, and, at 0.965 μm , it is 1.5, *i.e.*, about 30%
6 larger than with Model O-1. In the NIR, it remains almost constant, with a local
7 maximum at 1.35 μm and slightly decreasing beyond. However, the derived value
8 beyond 0.896 μm is at least 2.7 times larger than at 0.675 μm . This behavior, as it can be
9 seen when looking at the τ to Q_{ext} ratio, is not consistent with the extinction efficiency
10 factor provided by *Markiewicz et al.* [1999]. This could be due to dust in the canyon with
11 an optical parameter wavelength dependence different from that of Model M, in
12 particular, a dust darker (brighter) than Model M at wavelengths larger (smaller) than
13 0.896 μm . The haze optical depth derived by applying Models M-2 and M-3, although
14 larger in the NIR (10 to 25%) for M-2 and in the whole wavelength range for M-3 (7% in
15 the visible and up to 70% in the NIR), present a similar wavelength dependence to that
16 with Model M-1.

17

18 We finally derived the optical depth of the haze inside Valles Marineris with Models T-1,
19 T-2 and T-3. The results are shown in Figures 18-1 to 18-2. The optical depth of the haze
20 when using Model T-1 is slightly smaller at $\lambda \sim 0.6 \mu\text{m}$, similar at 0.7 μm and almost a
21 factor of 2 larger in the NIR than that derived with model O-1. Besides, the maximum
22 found in the optical depth, located at $\lambda = \sim 1.35 \mu\text{m}$, is more typical for the aerosol size
23 distributions usually measured in Mars [*e.g.*, *Clancy et al.*, 1995; *Drossart et al.*, 1991].
24 Therefore, Model T-1 provides a more reasonable optical depth wavelength dependence.

1 This better behavior of Tomasko-like-dust is also illustrated in Figure 18-2, which shows
2 that the ratio between τ and Q_{ext} remains constant with wavelength within a 20% range
3 (whereas that range was 50% with Model O-1). It is important to point out that the ratio
4 decreases monotonically towards longer wavelengths in the NIR, which could be an
5 indication of an incorrect assumption of constant optical properties in the whole NIR.
6 This could be balanced with a decrease (or increase) in the single scattering albedo (or of
7 the asymmetry parameter) in the NIR. It should also be noted that we have also
8 considered an extinction efficiency factor that is constant with wavelength, which is very
9 likely not to be a good assumption (but it should decrease with wavelength in the NIR).
10 Those two factors could decrease the slope of the ratio at $\lambda > 1.35 \mu\text{m}$.
11
12 The results with Model T-2 and T-3 are also shown in Figure 18-1. The results for the
13 optical depth in these cases are within 10% and 35% respectively of the ones derived with
14 Model T-1. The ratios of optical depth to extinction efficiency (shown in Figure. 18-2),
15 however, show a worse behavior than with Model T-1.

1 **5. Conclusions**

2
3 A haze was observed in Valles Marineris at $L_s \sim 40^\circ$ with HRSC and OMEGA on Mars
4 Express. The existence of multiangle and multispectral imaging for this haze allows haze
5 thickness, composition, and altitude to be determined, and models of aerosol optical
6 properties to be tested. The haze was observed to be brighter than bottom of the canyon in
7 visible wavelengths. The brightness decreased within three days and the haze disappeared
8 after nine days. The spectrometer detected no H₂O ice or CO₂ ice in absorption bands.
9 The spectral slope in NIR, however, indicates dust loading in the valley. The brightness
10 temperature of the feature is 223.77 ± 0.53 K. Therefore the composition of the haze was
11 dust.

12
13 Comparisons of reflectance detected with both instruments are useful for their cross
14 calibrations. OMEGA observes nadir in the nominal mode, while HRSC nine channels
15 point forward and backward along the orbit track. Also the panchromatic channels have
16 wide filters at a center wavelength of $0.675 \mu\text{m}$, where the reflectance of the Martian
17 surface increases with wavelength steeply. Therefore direct comparison requires careful
18 consideration of the scattering behavior of the surface and the atmosphere. The HRSC
19 Red I/F is larger than the OMEGA I/F, which is consistent with the results in *McCord et*
20 *al.* [2007]. The ratio of HRSC I/F to OMEGA I/F is 1.23, while the previously reported
21 value is 1.10. The difference is attributed as the scattering behavior with the different
22 geometric angles. Although there are slight shifts between the HRSC Green and Red
23 from the OMEGA spectra, we conclude that the measurements of the two instruments are
24 in agreement.

1

2

3 The characteristics of the dust layer are that;

4 (1) It is redder in the visible range than the surface below. The ratio of the reflectance at
5 $\lambda=0.75 \mu\text{m}$ to that at $\lambda=0.44 \mu\text{m}$ in the haze is 18% larger than that of the surface.

6 (2) It reflects diffusively relative to the surface that more effectively back scatters. Hence
7 the reflectance of the dust haze has a clear emission angle dependence, while that of the
8 surface depends more on the phase angles.

9 (3) The haze appeared below the altitude of -4200 ± 500 m. The haze seems to be
10 concentrated within lowest two km of the atmosphere within the canyon.

11 (4) It presents a negative spectral slope in the NIR (1.26 relative to $2.5 \mu\text{m}$) with 10-20%
12 larger than that of the surface.

13

14 We estimated the optical depth of the haze from the both the HRSC and OMEGA images
15 using SHDOM. Although the surface does not scatter diffusively, the limited number of
16 angular data points from the stereo channels are not enough to derive a surface phase
17 function. Hence we considered the surface to be Lambertian. Three separate estimates of
18 the Lambert albedo (A_L) were derived assuming that after the haze disappeared (1) the
19 atmosphere was dust-free, (2) the optical depth of the atmosphere was 0.5 at $\lambda=0.67 \mu\text{m}$,
20 and (3) that was 1.0 at $\lambda=0.67 \mu\text{m}$. The retrieval of optical depth is sensitive to aerosol
21 scattering model used. The phase function of *Markiewicz et al.* [1999] represents a
22 measured angular dependence of reflectance that differs from the one-term Henyey-
23 Greenstein models using asymmetry factors taken from *Tomasko et al.* [1999] and
24 *Ockert-Bell et al.* [1997] especially in the forward ($g > \sim 150^\circ$) and backward ($g < \sim 30^\circ$)

1 scattering ranges. None of them, however, were able to fit all the HRSC stereo data
2 simultaneously with the Lambertian approximation, which indicates that (1) the surface
3 below the haze is non-Lambertian and/or (2) the dust particles in Valles Marineris have
4 larger backscattering components than the phase functions we used. The dust scattering
5 properties after *Ockert-Bell et al.* [1997] and *Markiewicz et al.* [1999] provided
6 unexpected inconsistencies between τ and Q_{ext} in the near infrared and visible region,
7 respectively. It is more suitable to apply the single scattering albedo and the phase
8 function of dust particles derived by *Tomasko et al.* [1999] from IMP on the Mars
9 Pathfinder to the observed dust haze, although the wavelength coverage is limited. From
10 the HRSC nadir data, $\tau = 1.7\text{--}2.3$ at $\lambda=0.67$ assuming the $A_L = 0.08 - 0.15$. From the
11 OMEGA spectral data, by fixing a constant single scattering albedo and an asymmetry
12 factor in the NIR, we found that the optical depth increases with increasing wavelength,
13 with a maximum value of 2.2-2.6 at $\lambda=1.35 \mu\text{m}$, then decreases to 1.2-1.8 at $\lambda=2.4 \mu\text{m}$.
14
15

1 **Acknowledgements**

2

3 We thank the HRSC Experiment Teams at DLR Berlin and Freie Universität Berlin as
4 well as the Mars Express Project Teams at ESTEC and ESOC for their successful
5 planning and acquisition of data as well as for making the processed data available to the
6 HRSC Team. We acknowledge the effort of the HRSC Co-Investigator Team members
7 and their associates who have contributed to this investigation in the preparatory phase
8 and in scientific discussions within the team. We thank the OMEGA team at Institut
9 d’Astrophysique Spatiale (University Paris Sud). We would like to thank Francois Forget
10 and Stéphane Erard for reviews that greatly improved this paper. This work was partially
11 supported by JSPS Postdoctoral Fellowships for Research Abroad (AI), by a NASA Mars
12 Data Analysis Program grant to Caltech (AI), and by the German Aerospace Center
13 (DLR) under contract RD-RX/50QM0011/7A (MGC).

14

15

16

17

1 **References**

2 Bell, J. F., W. M. Calvin, M. E. OckertBell, D. Crisp, J. B. Pollack, and J. Spencer
3 (1996), Detection and monitoring of H₂O and CO₂ ice clouds on Mars, *J Geophys Res-*
4 *Planet*, 101(E4), 9227-9237.

5

6 Bibring, J.-P. (2004), OMEGA: observatoire pour la Mineralogie, l'Eau, le Glace
7 et l'Activité, SP-1240., *ESA Publication*, 37-49.

8

9 Bibring, J. P., et al. (2004), Perennial water ice identified in the south polar cap of Mars,
10 *Nature*, 428(6983), 627-630.

11

12 Bibring, J. P., et al. (2006), Global mineralogical and aqueous mars history derived from
13 OMEGA/Mars express data, *Science*, 312(5772), 400-404.

14

15 Bonello, G., J. P. Bibring, A. Soufflot, Y. Langevin, B. Gondet, M. Berthe, and C.
16 Carabetian (2005), The ground calibration setup of OMEGA and VIRTIS experiments:
17 description and performances, *Planet Space Sci*, 53(7), 711-728.

18

19 Clancy, R. T., S. W. Lee, G. R. Gladstone, W. W. Mcmillan, and T. Rousch (1995), A
20 New Model for Mars Atmospheric Dust Based Upon Analysis of Ultraviolet through
21 Infrared Observations from Mariner-9, Viking, and Phobos, *J Geophys Res-Planet*,
22 100(E3), 5251-5263.

23

24 Clancy, R. T., M. J. Wolff, and P. R. Christensen (2003), Mars aerosol studies with the

1 MGS TES emission phase function observations: Optical depths, particle sizes, and ice
2 cloud types versus latitude and solar longitude, *J Geophys Res-Planet*, 108(E9),
3 doi:10.1029/2003JE002058
4
5 Clark, R. N. (1981), Water Frost and Ice - the near-Infrared Spectral Reflectance 0.65-2.5
6 $\mu\text{-m}$, *J Geophys Res*, 86(NB4), 3087-3096.
7
8 Combes, M., et al. (1991), Martian Atmosphere Studies from the Ism Experiment, *Planet*
9 *Space Sci*, 39(1-2), 189-197.
10
11 Drossart, P., J. Rosenqvist, S. Erard, Y. Langevin, J. P. Bibring, and M. Combes (1991),
12 Martian Aerosol Properties from the Phobos Ism Experiment, *Ann Geophys*, 9(11), 754-
13 760.
14
15 Erard, S., J. Mustard, S. Murchie, J. P. Bibring, P. Cerroni, and A. Coradini (1994),
16 Martian Aerosols - near-Infrared Spectral Properties and Effects on the Observation of
17 the Surface, *Icarus*, 111(2), 317-337.
18
19 Evans, K. F. (1998), The spherical harmonics discrete ordinate method for three-
20 dimensional atmospheric radiative transfer, *J Atmos Sci*, 55(3), 429-446.
21
22 Forget, F., et al. (2007), Remote sensing of surface pressure on Mars with the Mars
23 Express/OMEGA spectrometer. Part I: retrieval method *submitted to J. Geophys. Res.*
24

1 Gerakines, P. A., J. J. Bray, A. Davis, and C. R. Richey (2005), The strengths of near-
2 infrared absorption features relevant to interstellar and planetary ices, *Astrophys J*,
3 *620*(2), 1140-1150.

4

5 Gwinner, K., F. Scholten, M. Spiegel, R. Schmidt, B. Giese, J. Oberst, R. Jaumann, G.
6 Neukum, and H. C.-I. Team (2005), Hochauflösende Digitale Geländemodelle auf der
7 Grundlage von Mars Express HRSC-Daten, *Photogrammetrie, Fernerkundung*,
8 *Geoinformation*, *5*, 387-394.

9

10 Hillier, J. K., B. J. Buratti, and K. Hill (1999), Multispectral photometry of the moon and
11 absolute calibration of the clementine UV/Vis camera, *Icarus*, *141*(2), 205-225.

12

13 Jaumann, R., et al. (2006), The High Resolution Stereo Camera (HRSC) Experiment on
14 Mars Express: Instrument Aspects and Experiment Conduct from Interplanetary Cruise
15 through the Nominal Mission, *submitted to Planetary and Space Research*.

16

17 Jouglet, D., F. Poulet, R. Milliken, J. Mustard, J. P. Bibring, Y. Langevin, B. Gondet, and
18 t. O. team (2006), Hydration state of the Martian surface as seen by Mars Express
19 OMEGA I - Analysis of 3 μ m hydration feature, *submitted to J. Geophys. Res.*

20

21 Langevin, Y., F. Poulet, J. P. Bibring, and B. Gondet (2005), Sulfates in the north polar
22 region of Mars detected by OMEGA/Mars express, *Science*, *307*(5715), 1584-1586.

23 Markiewicz, W. J., R. M. Sablotny, H. U. Keller, N. Thomas, D. Titov, and P. H. Smith
24 (1999), Optical properties of the Martian aerosols as derived from Imager for Mars
25 Pathfinder midday sky brightness data, *J Geophys Res-Planet*, *104*(E4), 9009-9017.

1
2 McCord, T. B., et al. (2007), The Mars Express High Resolution Stereo Camera
3 Spectrophotometric Data: Characteristics and Science Analysis, *submitted to J. Geophys.*
4 *Res.*
5
6 Melchiorri, R., et al. (2006), A simulation of the OMEGA/Mars Express observations:
7 Analysis of the atmospheric contribution, *Planet Space Sci*, 54(8), 774-783.
8 Neukum, G., and R. Jaumann (2004), The HRSC Co-Investigator and Experiment Team,
9 HRSC: The High Resolution Stereo Camera of Mars Express, *ESA Special Publication*,
10 *ESA SP-1240*, 17-35.
11
12 Ockert-Bell, M. E., J. F. Bell, J. B. Pollack, C. P. McKay, and F. Forget (1997),
13 Absorption and scattering properties of the Martian dust in the solar wavelengths, *J*
14 *Geophys Res-Planet*, 102(E4), 9039-9050.
15
16 OckertBell, M. E., J. F. Bell, J. B. Pollack, C. P. McKay, and F. Forget (1997),
17 Absorption and scattering properties of the Martian dust in the solar wavelengths, *J*
18 *Geophys Res-Planet*, 102(E4), 9039-9050.
19
20 Pimentel, G. C., P. B. Forney, and K. C. Herr (1974), Evidence About Hydrate and Solid
21 Water in Martian Surface from 1969 Mariner Infrared Spectrometer, *J Geophys Res*,
22 79(11), 1623-1634.
23
24 Pollack, J. B., M. E. Ockertbell, and M. K. Shepard (1995), Viking Lander Image-

1 Analysis of Martian Atmospheric Dust, *J Geophys Res-Planet*, 100(E3), 5235-5250.

2 Scholten, F., et al. (2005), Mars express HRSC data processing - Methods and
3 operational aspects, *Photogramm Eng Rem S*, 71(10), 1143-1152.

4

5 Smith, M. D., J. C. Pearl, B. J. Conrath, and P. R. Christensen (2001), One Martian year
6 of atmospheric observations by the Thermal Emission Spectrometer, *Geophysical*
7 *Research Letters*, 28(22), 4263-4266.

8

9 Smith, M. D. (2004), Interannual variability in TES atmospheric observations of Mars
10 during 1999-2003, *Icarus*, 167(1), 148-165.

11

12 Tomasko, M. G., L. R. Dose, M. Lemmon, P. H. Smith, and E. Wegryn (1999),
13 Properties of dust in the Martian atmosphere from the Imager on Mars Pathfinder, *J*
14 *Geophys Res-Planet*, 104(E4), 8987-9007.

15

16 Wang, H. Q., and A. P. Ingersoll (2002), Martian clouds observed by Mars Global
17 Surveyor Mars Orbiter Camera, *J Geophys Res-Planet*, 107(E10), art. no.-5078.

18 Warren, S. G. (1984), Optical-Constants of Ice from the Ultraviolet to the Microwave,
19 *Appl Optics*, 23(8), 1206-1225.

20

21 Yen, A. S., B. C. Murray, and G. R. Rossman (1998), Water content of the Martian soil:
22 Laboratory simulations of reflectance spectra, *J Geophys Res-Planet*, 103(E5), 11125-
23 11133.

24

1

2

3

1 **Figure Captions**

2

3 Fig. 1 HRSC true color images of Valles Marineris obtained on 25 May 2004 (during
4 orbit 438, $L_s = 38^\circ$, LT = 09:15, right), 28 May 2004 (449, $L_s=40^\circ$, LT=09:15, middle)
5 and 3 June 2004 (471, $L_s=42^\circ$, LT=09:00, left). The red and white lines are along
6 longitudes of 298.7°E and 301.2°E respectively. The boxes indicate the north region
7 ($12.00^\circ\text{S} - 12.25^\circ\text{S}$, $302.0^\circ\text{E}-302.5^\circ\text{E}$) and the inside of the valley ($13.75^\circ\text{S}-14.00^\circ\text{S}$,
8 $302.0^\circ\text{E}-302.5^\circ\text{E}$).

9

10

11 Fig. 2 Brightness across Valles Marineris acquired with the HRSC Green channel. The
12 dotted lines show the altitude for the reference. Left: I/F along the longitude of 301.2°E ,
13 solid and dotted lines are for orbits 438 and 449. Right: I/F along the longitude of
14 298.8°E , solid and dotted lines are for orbit 449 and 471.

15

16 Fig. 3 Left: Reflectance of the inside valley and north sub-regions (Fig. 1) detected by
17 OMEGA are given as the solid and dotted lines, while those obtained by HRSC are as the
18 asterisks and the diamonds respectively. The thermal emission and atmospheric gaseous
19 absorptions are corrected after *Jouglet et al.* [2006] and *Langevin et al.* [2005],
20 respectively. The shadow areas represent one standard deviation of OMEGA data. Right:
21 As in the left plot, but enlarged in the visible wavelength region.

22

23 Fig. 4-1 Relative band depth maps around Valles Marineris at wavelength of the CO_2 ice
24 absorption band at $1.43 \mu\text{m}$ acquired by OMEGA during orbit 438 (a) and 482 (b). The

1 wavelengths chosen for the local continuum are 1.39 and 1.44 μm .

2

3 Fig. 4-2 Relative band depth maps of the H_2O ice absorption band at 1.50 μm acquired by
4 OMEGA during orbits 438 (a) and 482 (b) over Valles Marineris. The band depth is
5 smaller than 2%, which indicates that no water ice was detected.

6

7

8 Fig. 4-3 Normalized integrated water band depth at the wavelength of 3.0 μm observed
9 during orbit 438 (a) and 482 (b). They include the information of the hydration of the
10 surface and the water amount over it. The variation between inside and outside of the
11 valley is less than 3 %.

12

13 Fig. 4-4 Water content of the surface and the atmosphere detected at the wavelength of
14 3.0 μm during orbit 438 (a) and 482 (b). Its variation over this area is less than 3 %.

15

16 Fig. 4-5 The ratio of I/F at 1.26 μm to I/F at 2.49 μm measured by OMEGA during orbits
17 438 (a) and 482 (b). A sharp decrease in I/F with wavelength in the NIR is an indication
18 of dust loading. Orbit 438 presents a clearly steeper (negative) slope in the spectra where
19 HRSC detected the haze inside Valles Marineris.

20

21 Fig. 5 Brightness temperature vs. local time derived with the thermal corrected data
22 measured by OMEGA. The selected longitudes are 302.10°E, 298.94°E and 298.73°E for
23 orbit 438 (local time 09:15), 460 (09:07) and 482 (08:53) respectively. The brightness
24 temperature is averaged in 0.1 x 0.1 deg. boxes. The error bars represent 1-sigma

1 standard deviation. The brightness temperature of the north and inside of the valley are
2 shown as the solid and dashed lines respectively.

3

4 Fig. 6 I/F color slopes of region 1 observed by HRSC on orbits 438 (the solid line), 449
5 (dotted), region 2 on orbits 449 (dashed), and 471 (dot-dashed). Two images overlapped
6 these regions. Regions 1 and 2 are at $(14.25 \pm 1.75^\circ \text{S}, 301.2 \pm 0.5^\circ \text{E})$ and $(13.5 \pm 1.5^\circ \text{S},$
7 $298.7 \pm 0.5^\circ \text{E})$, respectively. The error bar shows 1-sigma level.

8

9 Fig. 7 Color-composite stereo images of region 1 of orbit 438 (upper left), orbit 449
10 (upper right) and region 2 of orbit 449 (lower left) and orbit 471 (lower right). S1 is red,
11 nadir is green and S2 is blue. The rectangles are selected regions to compare I/F of inside
12 and outside of Valles Marineris. R1-N and R1-In denote the areas of north and inside of
13 Valles Marineris in region 1 respectively, while R2-N and R2-In are for the areas of north
14 and inside of the valley in region 2.

15

16 Fig. 8 The angular dependences of the reflectance from region 1 in orbit 438 (the solid
17 line with asterisks), orbit 449 (the solid line with diamonds), region 2 in orbit 449 (the
18 dashed line with diamonds) and orbit 471 (the dashed line with triangles) detected by
19 HRSC. The upper panels show the emission angle dependence, while the lower panels
20 show the phase angle dependence. The left and right panels give the mean I/F only inside
21 the valley (given as R1-In and R2-In in Fig. 7) and the outside (R1-N and R2-N)
22 respectively.

23

24 Fig. 9 The HRSC blue image of orbit 437 with the haze edge against the northern wall of

1 Valles Marineris. The edge was defined as $0.0445 < I/F < 0.0460$.

2

3 Fig. 10 Cross section of the DTM along the longitude of 302°E . The arrows indicate the
4 boarder of the haze.

5

6 Fig. 11 Altitude of the main haze edge against the northern wall detected on orbit 438.
7 The mean height is -4172 ± 531 m.

8

9 Fig. 12 The solid line is for the phase function of dust particles presented by *Markiewicz*
10 *et al.* [1999]. The dashed and the dot-dashed lines are the Henyey-Greenstein phase
11 function with the asymmetry factors after *Tomasko et al.* [1999] and *Ockert-Bell et al.*
12 [1997]. All phase functions are calculated at the wavelength of $0.675 \mu\text{m}$.

13

14 Fig. 13 Single scattering albedos of dust particles (left) and asymmetry factors of dust
15 phase functions (right). The solid line is after *Markiewicz et al.* [1999], the dashed is after
16 *Tomasko et al.* [1999] and the dot-dashed line is after *Ockert-Bell et al.* [1997]. The
17 dotted lines are assumed for this study.

18

19

20 Fig. 14 Left column: I/F calculated at various optical depth (τ) (lines) are compared with
21 the observed I/F obtained by the HRSC panchromatic channels (diamonds). The interval
22 of τ is 0.5 and the angular geometry follows to that of each data points. The surface
23 Lambert albedo (A_L) is 0.15. Right column: Contour map of I/F with $0.0 < A_L < 0.2$ and
24 $0.0 < \tau < 5.0$. The incidence angle of 49.4 deg. , the emission angle of 3.79 deg. , and the

1 phase angle of 46.0 deg. corresponding to the geometry of the nadir channel are applied.
2 The aerosol scattering models of (top) *Markiewicz et al.* [1999] (middle) *Tomasko et al.*
3 [1999] and (bottom) *Ockert-Bell et al.* [1997] are employed.

4

5 Fig 15. OMEGA average I/F (solid) and $I/(F \times \cos(i))$ (dashed) spectra for orbits 438
6 (diamonds) and 482 (triangles) inside a $0.4^\circ \times 1^\circ$ box in Valles Marineris. The feature
7 exhibited at $1.5 \mu\text{m}$ results from an instrumental effect due to the non-linearity of the
8 detector. The spectra are atmospherically corrected. Nevertheless, some artifacts are still
9 present in the $2.0 \mu\text{m}$ wavelength region due to strong CO_2 absorption bands.

10

11 Fig 16. Lambert albedo derived from OMEGA data for orbit 482 (solid: considering an
12 aerosol-free scenario; dashed: considering an optical depth of 0.5; dotted: considering an
13 optical depth of 1.0 and assuming dust properties after *Ockert-Bell et al.* [1997] (red),
14 *Markiewicz et al.* [1999] (black), and *Tomasko et al.* [1999] (blue)).

15

16 Fig. 17-1. Dust optical depth (solid line) for orbit 438 using *Ockert-Bell et al.* [1997]
17 optical properties and an albedo derived from orbit 482 assuming a Lambertian-surface
18 and aerosol-free scenario. The shadowed region shows the error in the optical depth
19 calculated with the error range in the dust single scattering albedo and phase function
20 asymmetry parameter provided by Ockert-Bell.

21

22 Fig. 17-2. Ratio between Ockert-Bell-like dust optical depth (shown in Fig. 17-1) and
23 Ockert-Bell's extinction coefficient for orbit 438. The shadowed area shows the
24 estimated error in the ratio assuming Ockert-Bell's optical parameters errors.

1

2 Fig 18-1. Optical depth retrieved from OMEGA data for orbit 438 inside Valles
3 Marineris. The symbols (grouped in pairs) correspond to the three different dust models
4 used: *Ockert-Bell et al.* [1997] (red), *Markiewicz et al.* [1999] (black), and *Tomasko et*
5 *al.* [1999] (blue). For each of three aerosol models assumed, the optical depths were
6 obtained using an input Lambert albedo derived from orbit 482 under three different
7 cases: assuming an aerosol-free scenario (solid), and assuming optical depths of 0.5
8 (dashed) and 1.0 (dotted) at 0.675 μm (see text).

9

10 Fig. 18-2. Ratio between the retrieved optical depth for orbit 438 shown in Fig. 18-1 and
11 the extinction coefficient. The color and the style of lines denote the same in Fig. 18-1.

1 **Table**

2

3 **Table 1** Summary of Observations. *i*, *e* and *g* are average incidence, emission and phase
 4 angles of the Valles Marineris data respectively. S1, IR, P1, GR (Green), ND, BL (Blue),
 5 P2, RE (Red) and S2 denotes the HRSC channels.

Orbit Number	Instrument	Observation Day	Ls [deg]	Local Time	<i>i</i> [deg]	<i>e</i> [deg]	<i>g</i> [deg]
438	HRSC	25-May-04	38	9:15	49	28 (S1), 23 (IR), 18 (P1), 6 (GR), 4 (ND), 7 (BL), 19 (P2), 24 (RE), 28 (S2)	66(S1), 63(IR), 60(P1), 51(GR), 49(ND), 46(BL), 41(P2), 40(RE), 39(S2)
438	OMEGA	25-May-04	38	9:15	49	10	49
449	HRSC	28-May-04	40	9:15	51	28(S1), 23(IR), 7(GR), 5(ND), 8(BL), 24(RE), 29(S2)	65(S1), 62(IR), 50(GR), 47(ND), 45(BL), 38(RE), 38(S2)
460	OMEGA	31-May-04	41	9:07	53	9	52
471	HRSC	3-Jun-04	42	9:00	53	26(S1), 22(IR), 6(GR), 4(ND), 7(BL), 25(RE), 30(S2)	67(S1), 64(IR), 54(GR), 51(ND), 49(BL), 42(RE), 41(S2)
482	OMEGA	6-Jun-04	45	8:57	55	12	55

6

7

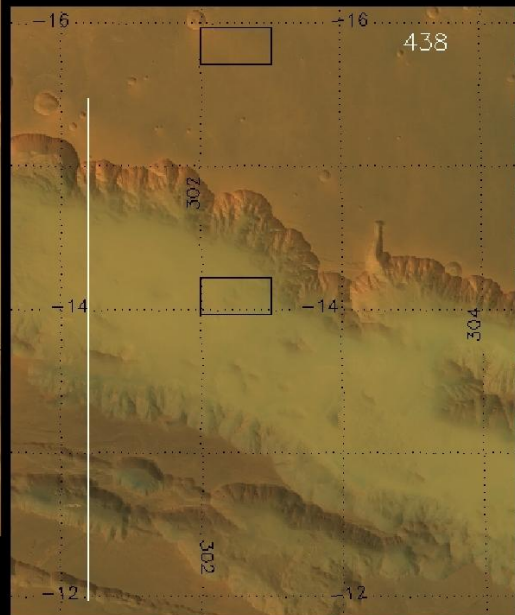
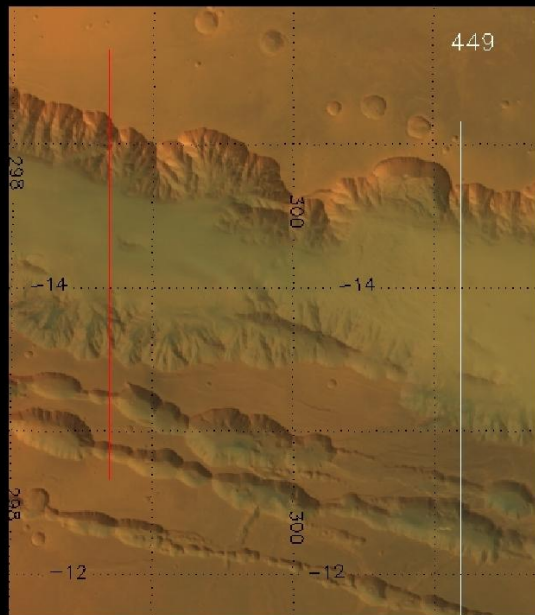
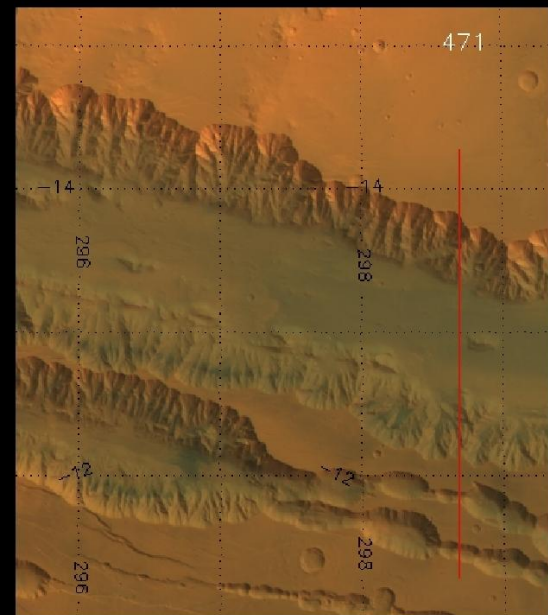
8

9

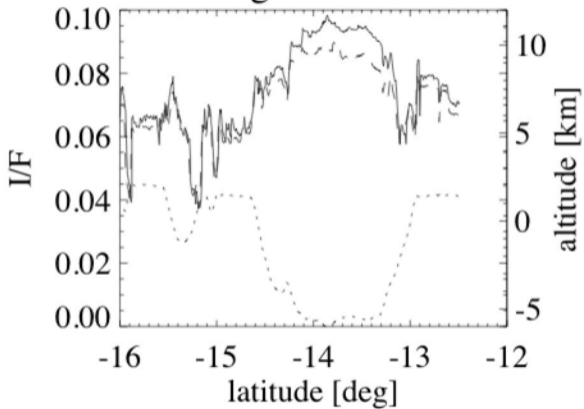
- 1 **Table 2** Applied Scattering Models and the Derived Optical Depth of the Haze with
 2 HRSC. τ and λ denote the optical depth and the wavelength in unit of μm .

Model	τ at $\lambda = 0.67$ on orbit 471	A_L at $\lambda = 0.67$	Haze τ at $\lambda = 0.67$ with HRSC ND data	reference
M-1	0.0	0.15	3.6	Markiewicz <i>et al.</i> [1999]
M-2	0.5	0.14	3.7	Markiewicz <i>et al.</i> [1999]
M-3	1.0	0.12	3.9	Markiewicz <i>et al.</i> [1999]
T-1	0.0	0.15	1.7	Tomasko <i>et al.</i> [1999]
T-2	0.5	0.13	1.9	Tomasko <i>et al.</i> [1999]
M-3	1.0	0.08	2.3	Tomasko <i>et al.</i> [1999]
O-1	0.0	0.15	1.9	Ockert-Bell <i>et al.</i> [1997]
O-2	0.5	0.13	2.1	Ockert-Bell <i>et al.</i> [1997]
O-3	1.0	0.08	2.5	Ockert-Bell <i>et al.</i> [1997]

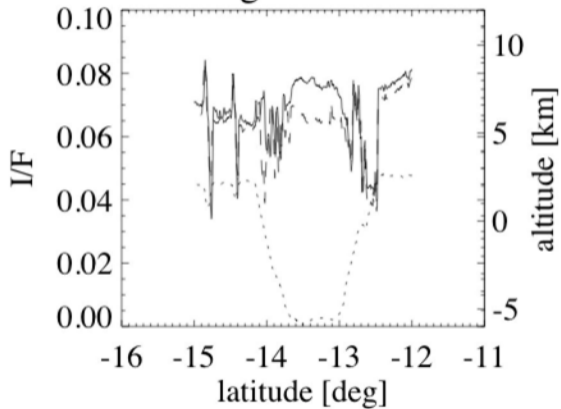
- 3
 4
 5
 6
 7
 8
 9
 10
 11

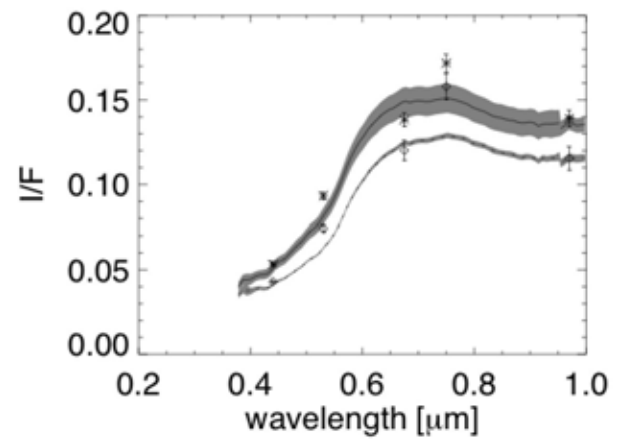
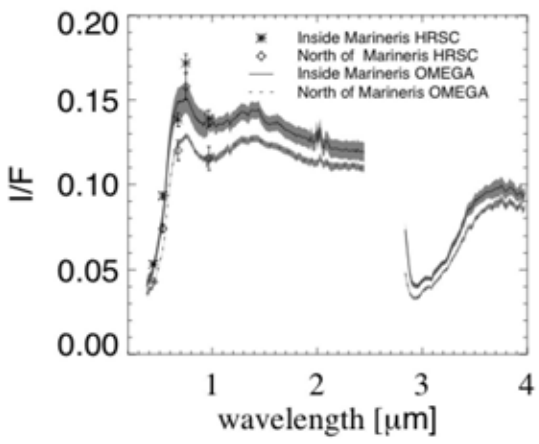


along lon=301.2

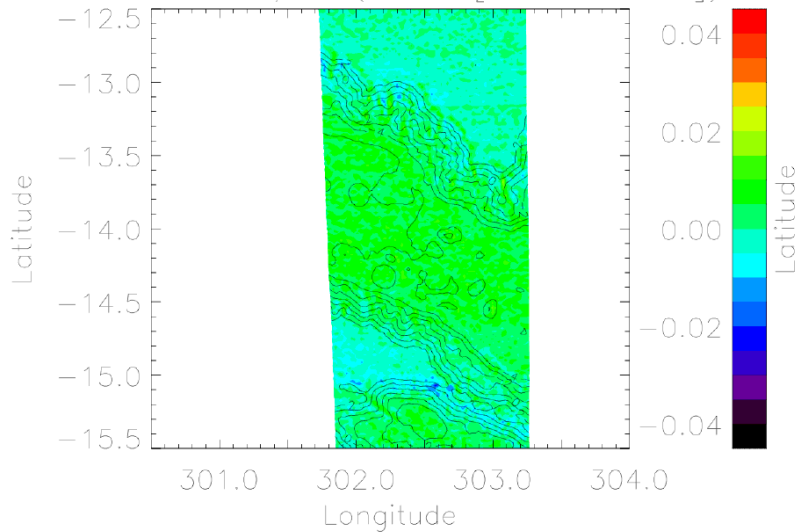


along lon=298.7

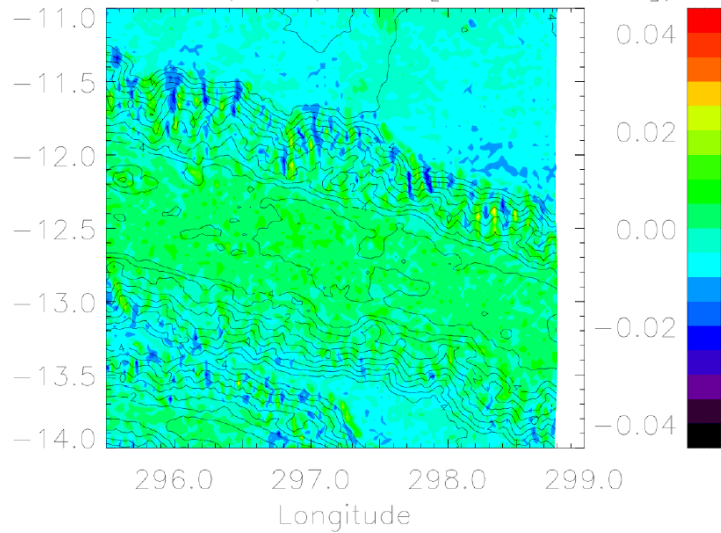




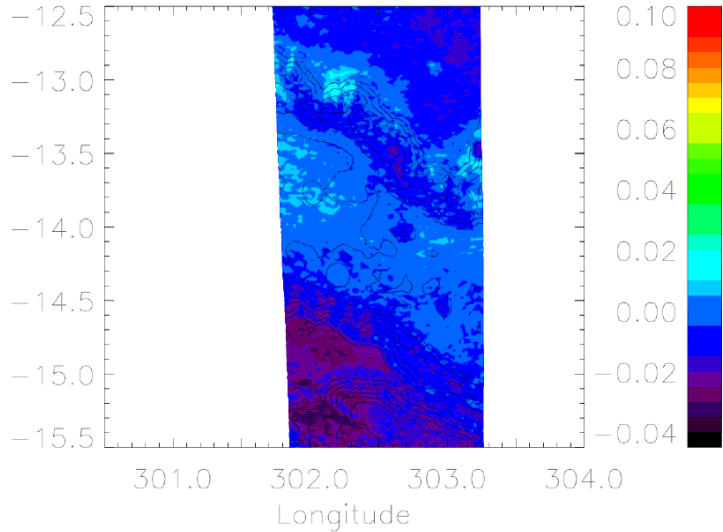
a) RBD at $1.43\mu\text{m}$ (cont=[1.39, 1.44])



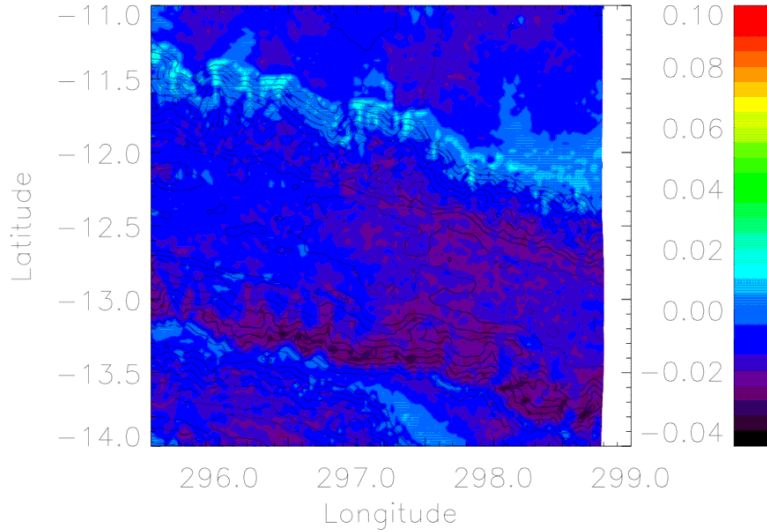
b) RBD at $1.43\mu\text{m}$ (cont=[1.39, 1.44])



a) RBD at $1.50\mu\text{m}$ (cont= $[1.30, 1.71]$)

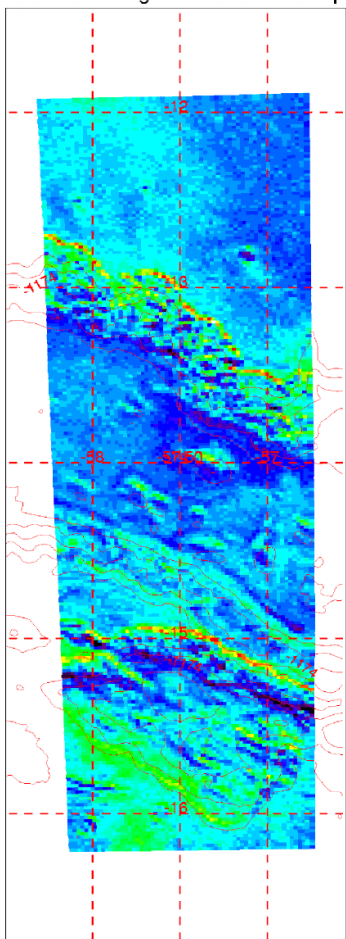


b) RBD at $1.50\mu\text{m}$ (cont= $[1.30, 1.71]$)



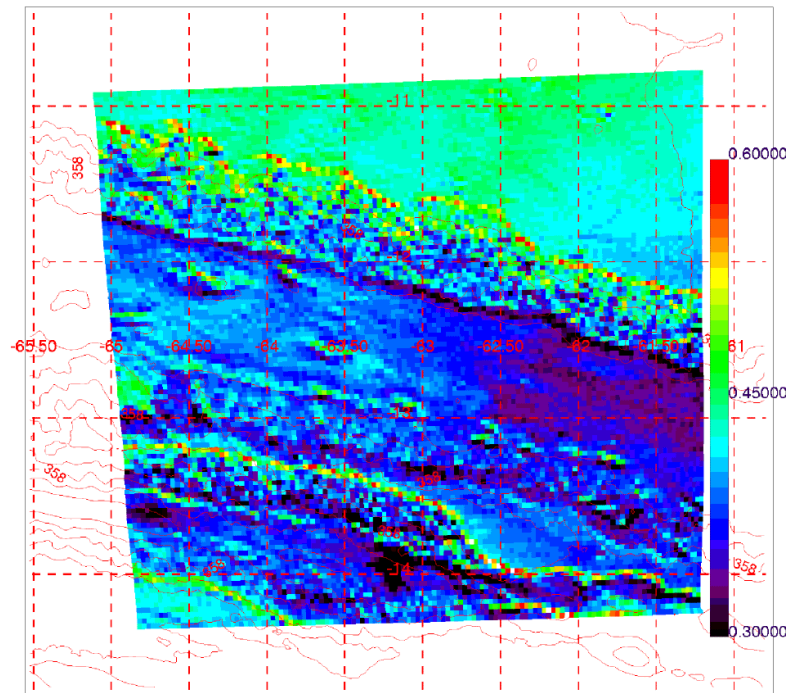
a)

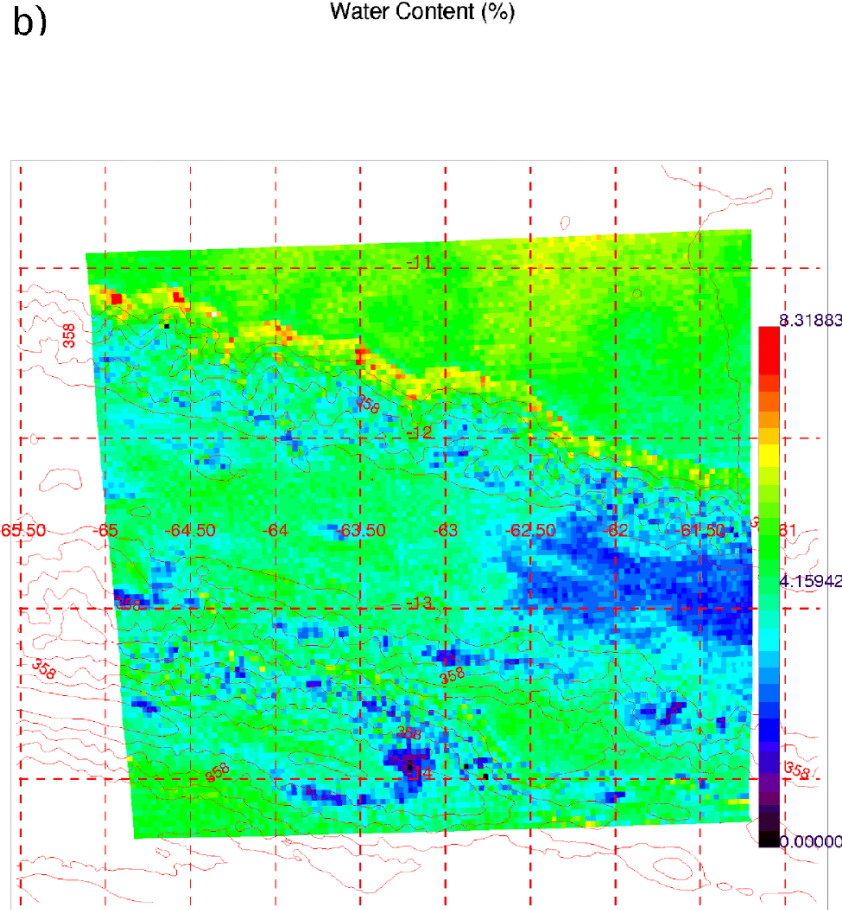
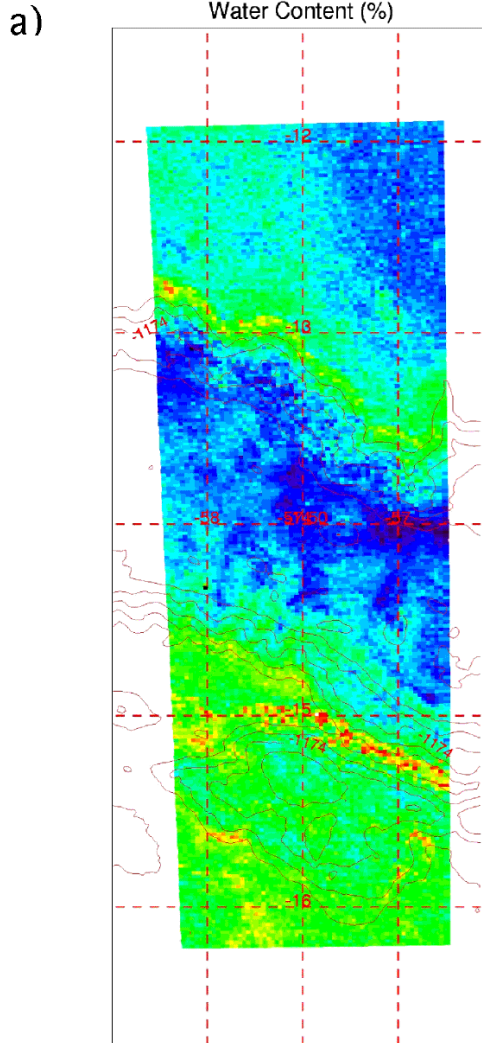
Normalized integrated water band depth



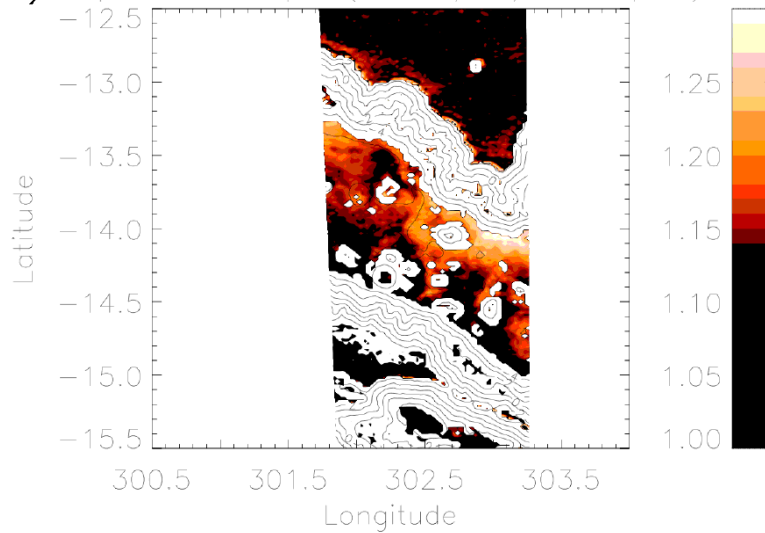
b)

Normalized integrated water band depth

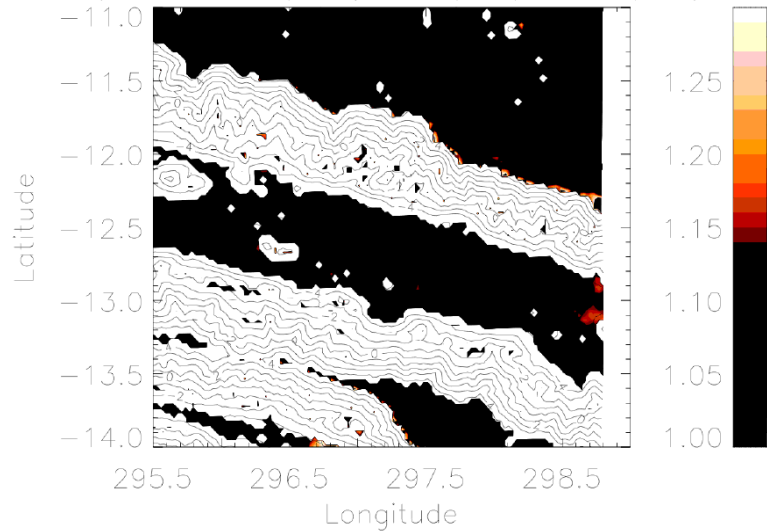


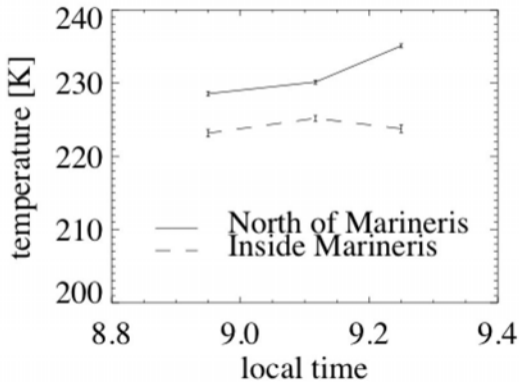


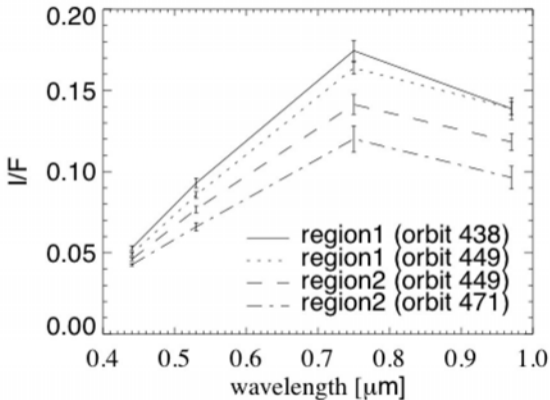
a) Spectral slope ($1.26\mu\text{m}/2.49\mu\text{m}$)



b) Spectral slope ($1.26\mu\text{m}/2.49\mu\text{m}$)

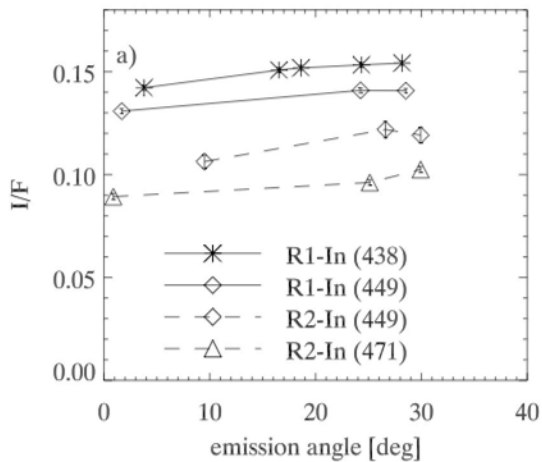








inside Marineris



outside of Marineris

